ARTM CHANNEL SOUNDING RESULTS – AN INVESTIGATION OF FREQUENCY SELECTIVE FADING ON AERONAUTICAL TELEMETRY CHANNELS

Michael Rice, David de Gaston, Adam Davis, Gus German, Christian Bettwieser
Department of Electrical and Computer Engineering
Brigham Young University

ABSTRACT

Initial results of wideband channel sounding experiments sponsored by the Advanced Range Telemetry (ARTM) program are presented. Data collected at Edwards EAFB during the Winter 1998-1999, are analyzed in the frequency domain to estimate the number, strength, and delays of the significant multipath reflections observed during the experiments. We observe that the channel is adequately modeled using two or three multipath reflections. The multipath fade events are correlated with recorded bit error rates and transmitter location to provide a comprehensive overview of the channel characteristics. Summaries from two test flights are included where it is seen that the 2- and 3-ray channel models provide excellent models for the data. In general, the 3-ray model captures the essential features of the multipath interference. In this model the first multipath is a strong specular reflection with relative amplitude greater than 0.5 and relative delay in the 30 to 70 ns range. The second multipath is a much weaker reflection with relative amplitude less than 0.5 and relative delay in the 175 to 325 ns range.

KEY WORDS

Channel Sounding, Channel Characterization, Multipath Fading, ARTM.

INTRODUCTION

Multipath interference occurs when reflected replicas of the transmitted wave front arrive within the main lobe of the receive antenna gain pattern [12]. The random phasing of these reflections causes random periods of constructive and destructive interference. When the destructive interference reduces the carrier-to-noise ratio at the receiver front end to an unacceptably low level, a multipath fade event occurs which produces what is often called a “data outage” or “signal outage” [1].

Mitigation techniques for fading include space diversity, antenna diversity [2], interleaved error control coding [3], and equalization [3]. The effectiveness of these

techniques depends on certain fading characteristics such as the number, strength and time delays of these reflections. One of the tasks of the Advanced Range Telemetry (ARTM) Program is to investigate the properties of multipath fading in common aeronautical telemetry environments. This paper reports on the initial results from two ARTM channel sounding flights at Edwards AFB in December 1998 and February 1999.

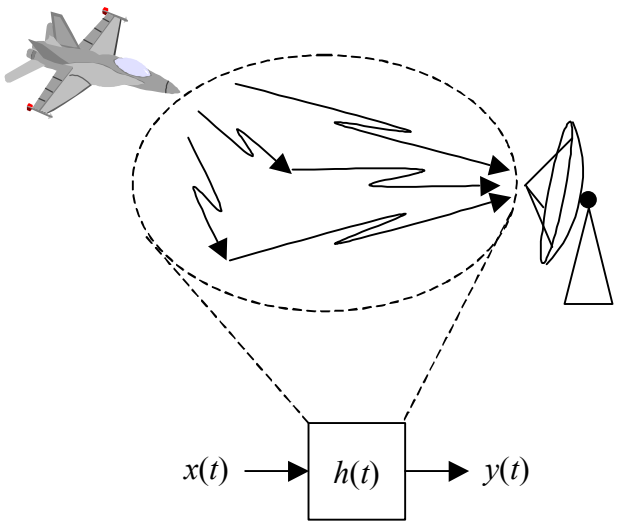

$Y(f) = H(f)X(f)$

Figure 1: Linear time-invariant system representation of the RF multipath environment.

CHANNEL MODELS AND SOUNDING TECHNIQUES

We begin by noting that real channels are *time-varying*. The channel impulse response is a function of the physical geometry involving the airborne transmitter, the receiver, and the reflection points. Since this geometry varies during the mission, the channel impulse response varies during the mission. The characterization of these changes or channel dynamics, is treated in [4]. We assume that over a short enough time interval, the channel does not change and is time-invariant. Thus, during a sufficiently short interval of time, we model the aeronautical telemetry channel as a linear, time-invariant system with impulse response $h(t)$ and transfer function $H(f)$ as illustrated in Figure 1. When a signal $x(t)$ is input to the system, the channel output $y(t)$ is given by the convolution of $x(t)$ with $h(t)$. In the frequency domain, the input-output relationship is $Y(f) = H(f)X(f)$.

Observations of received signal properties at Point Mugu NAWC [5,6], White Sands Missile Range [7], Edwards AFB [8,9], and China Lake NAWC [10] suggest that a good model for the aeronautical telemetry channel is one consisting of a line-of-sight signal accompanied by a single strong specular reflection whose delay relative to the line-of-sight signal is some fraction of the bit time. Such a channel is modeled mathematically as

$$h(t) = d(t) + \Gamma e^{j(2pf_0 t + q)} d(t - t) \qquad (1)$$

where $0 \le \Gamma \le 1$ is the strength of the reflection relative to the line-of-sight signal, θ is the phase shift caused by the reflective medium, τ is the delay of the specular reflection, and $2pf_0t$ is the phase shift caused by the delay (f_0 is the carrier frequency). Γ and θ are a function of the permeability, permittivity, and roughness of the reflecting surface, the incidence angle of the arriving electromagnetic wavefront [11], and the gain of the receive antenna in the direction of the arriving specular reflection [12]. The relative delay τ is a function of the geometry: slant range, elevation angle, etc. The overall phase shift of the specular reflection is $g = 2pf_o t + q$. For our analysis, we are interested only in γ and not in its constituent parts so that

$$h(t) = d(t) + \Gamma e^{jg} d(t - t). \tag{2}$$

The magnitude of the corresponding channel transfer function is

$$|H(f)|^2 = 1 + \Gamma^2 + 2\Gamma\cos(2pft - g). \tag{3}$$

Some of the data to be presented later is well modeled by a channel consisting of two specular reflections. In this case we have

$$h(t) = d(t) + \Gamma_1 e^{jg_1} d(t - t_1) + \Gamma_2 e^{jg_2} d(t - t_2) \tag{4}$$

where the subscripts are used to denote the magnitude, phase shift, and delay of the first and second reflections. In general, a multipath channel with L reflections may be modeled as an LTI system with impulse response

$$h(t) = d(t) + \sum_{i=1}^{L} \Gamma_i e^{jg_i} d(t - t_i). \tag{5}$$

In many applications, the accuracy of the model improves with increasing L. But models with large L are of limited practical value in simulation and analysis. Thus we prefer channel models with as small an L as possible. Our data modeling shows excellent results using $L = 1$ or 2.

The ideal channel sounder is one that transmits an impulse and records the channel output. When $x(t) = \delta(t)$, $y(t) = h(t)$. Since transmitting an ideal impulse is not possible, the alternative method outlined in Figure 2 is often used. Here $x(t)$ is a bipolar NRZ pseudo-random (PN) sequence of length M. The PN sequence is used because it has the desirable correlation property [13]:

$$\begin{aligned} R_{XX}(l) &= \int_{-\infty}^{\infty} x(t)x(t+l)dt \\ &= \begin{cases} 1 - \dfrac{|l|}{T_c}\left(1 + \dfrac{1}{M}\right) & |l| \le T_c \\ -\dfrac{1}{M} & T_c < |l| < (M-1)T_c \end{cases} \end{aligned} \tag{6}$$

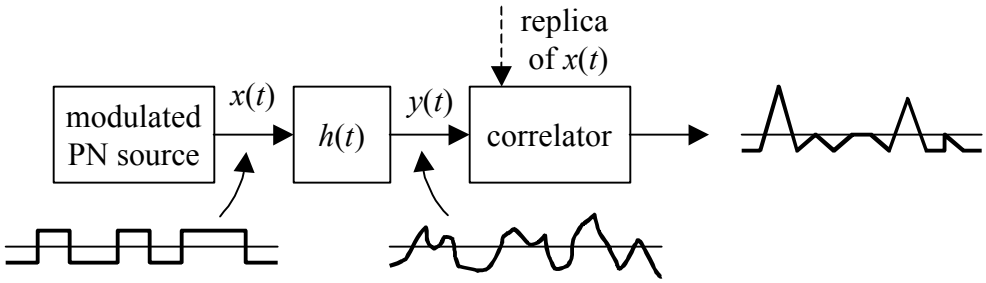

Figure 2: PN sequence method for channel sounding. The received signal is correlated with a locally generated replica of the transmitted modulated PN sequence. The resulting correlation peaks identify the multipath reflections.

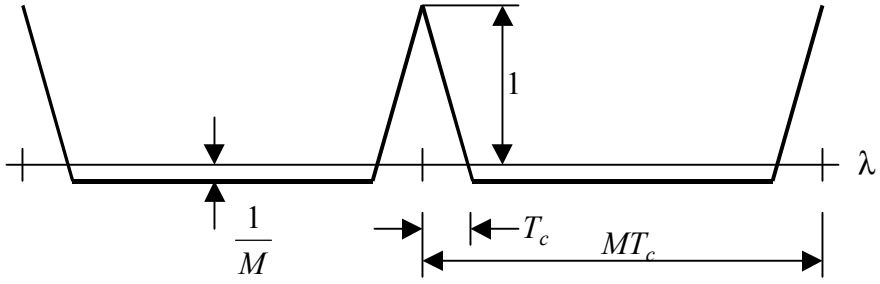

Figure 3: Periodic correlation function for length-M PN sequence modulated with bipolar NRZ pulse shape with a bit period of T_c seconds.

where T_c is the bit period. A plot of the correlation function (6) is shown in Figure 4 where it is seen that it is periodic with period T_c.

To see how channel sounding is accomplished using a signal with this property, consider what happens when x(t) is passed through a two ray channel with impulse response given by equation (2). In this case, $y(t) = x(t) + \Gamma e^{jg} x(t - t)$. The channel sounding procedure computes the cross correlation between the received signal $y(t)$ and the transmitted PN sequence $x(t)$:

$$\begin{aligned} R_{YX}(l) &= \int_{-\infty}^{\infty} y(t)x(t + l)dt \\ &= R_{XX}(l) + \Gamma e^{jg} R_{XX}(l - t) \end{aligned} \tag{7}$$

The cross correlation function is plotted in Figure 4 for two important cases. In the first case, $\tau > 2T_c$ so that the correlation peaks do not overlap. From the cross correlation function, we are able to determine the magnitude, phase, and delay of the reflection. In the second case, $\tau < 2T_c$ so that the two correlation peaks overlap thereby making the determination of the reflection properties problematic.

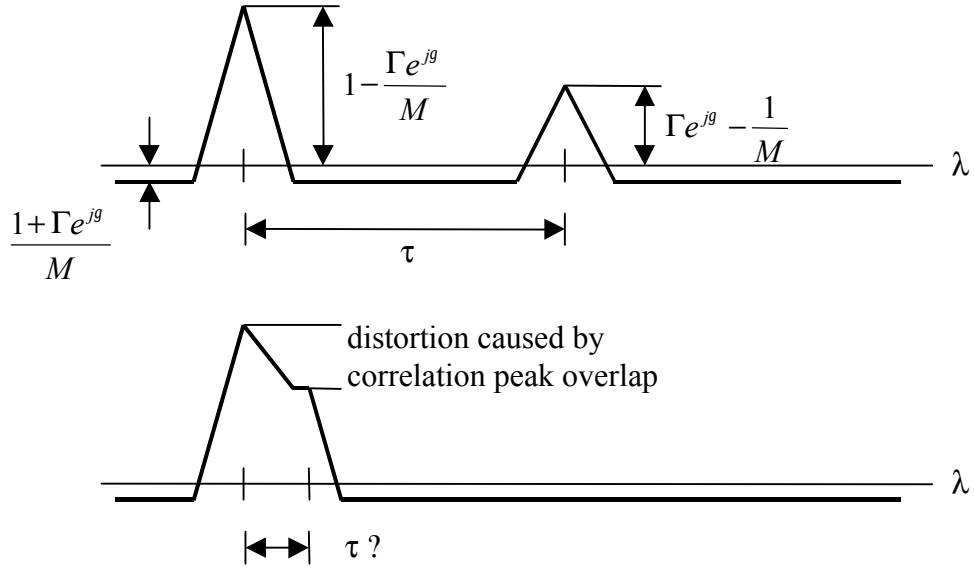

Figure 4: Examples of the cross correlation between the transmitted length-*M* PN sequence and the output of a 2-ray channel with impulse response given by Equation (3). The top figure illustrates the case where the delay τ is greater than $2T_c$. Two distinct peaks are obvious and are separated by the time delay τ. The bottom figure illustrates the case where τ is less than $2T_c$. The two correlation peaks are smeared together making the identification of the channel parameters problematic.

When $\tau < 2T_c$ it is still possible to perform some channel modeling using frequency domain techniques. This technique uses the power spectral densities of the input and output signals which we denote by $S_X(f)$ and $S_Y(f)$, respectively, and exploits the relationship

$$S_Y(f) = |H(f)|^2 S_X(f). \tag{8}$$

Using this technique, the power spectral density of the received signal is computed then divided by the power spectral density of the known transmitted signal (the PN sequence in our case) to obtain an estimate of the magnitude of the channel transfer function (which we call $|\hat{H}(f)|$):

$$|\hat{H}(f)|^2 = \frac{S_Y(f)}{S_X(f)}. \tag{9}$$

As an illustration of the technique, assume a 2-ray channel model $h(t)$ given by (2) with corresponding transfer function given by (3). The channel transfer function $H(f)$ is completely specified by the three parameters Γ, γ, and τ. The parameters that most closely match the data may be determined by choosing the parameters to minimize the squared error between the assumed transfer function $|H(f)|^2$ and the measured transfer function $|\hat{H}(f)|^2$. Usually, some weighting is used so that small values of $|H(f)|^2$ and

$\left|\hat{H}(f)\right|^2$ are not ignored by the curve fitting process. For example, Rummler [14] divided each point by the square of its absolute value. Here we use a different weighting by converting the data to decibels (dB) to convert equal magnitude differences to linear differences. In this way, the structure of 20 to 30 dB nulls in $\left|\hat{H}(f)\right|^2$ are preserved in the curve fit. In mathematical terms, the best-fit parameters are expressed as

$$(\Gamma, g, t)_{\text{opt}} = \underset{(\Gamma, g, t)}{\arg\min} \left\{ \left(20\log|H(f)| - 20\log\left|\hat{H}(f)\right| \right)^2 \right\} \tag{10}$$

where the conversion to dB has been made explicit. The extension of this technique to the 3-ray model is straight forward. Since many of the delays encountered during the ARTM channel sounding experiments were less than T_c, the frequency domain method was used to process the data.

EXPERIMENTAL CONFIGURATION

The channel sounding experiments were conducted as outlined in Figure 5. A length-127 PN sequence was transmitted using a 10 Mbit/second BPSK transmitter in a T-39 aircraft. A 2-Watt linear power amplifier was connected to a linearly polarized antenna mounted under the fuselage. A GPS receiver logged the time and position for post flight data correlation. The receiving station was located at Building 5790, the main telemetry receiving site at the Edwards AFB complex. The receiver was equipped with a circularly polarized tracking antenna, a wideband telemetry receiver with a linear 70 MHz IF output, and data acquisition equipment. The receiver AGC signal was sampled at a rate of 50 ksamples/second and recorded with GPS derived time stamps. The bit error counts from the bit error rate analyzer were also logged.

The IF output was sampled at a rate of 100 Msamples/second using a high-speed digital oscilloscope. The oscilloscope sampling-trigger was driven by a BPSK demodulator coupled with a bit error rate analyzer. Whenever the bit error count exceeded a certain level, the sample trigger was asserted. During each trigger event, the digital oscilloscope recorded 10 evenly spaced data segments. Each segment consisted of 10,000 samples, or 100 μseconds of data. At the end of each trigger event, the samples were downloaded from the digital oscilloscope to a PC and logged with a time stamp.

To apply the frequency domain curve fitting techniques of Equations (9) and (10) to the sampled data, careful associations must be made between the recorded discrete-time data and the continuous-time data assumed by the technique. This association is outlined in Figure 6. Here we see that we have samples of the output signal $y(t)$ which we denote $y(nt_s)$ where t_s = 10 ns is the sample period. Computing the N-point DFT of the sequence $y(nt_s)$ produces $Y_d\left(e^{j\Omega}\right)\Big|_{\Omega=\frac{2pk}{N}}$ for $k = 0,1,\ldots,N\text{-}1$ where $Y_d\left(e^{j\Omega}\right)$ is the discrete-time Fourier

transform (DTFT) of $y(nt_s)$ and $-p < \Omega \le p$ is the discrete-time frequency. Using samples of the input signal $x(nt_s)$ we can compute $\left|X_d\left(e^{j\Omega}\right)\right|^2$ and form the ratio

$$\left|H_d\left(e^{j\Omega}\right)\right|^2_{\Omega=\frac{2pk}{N}} = \left.\frac{\left|Y_d\left(e^{j\Omega}\right)\right|^2}{\left|X_d\left(e^{j\Omega}\right)\right|^2}\right|_{\Omega=\frac{2pk}{N}} \qquad \text{for } k = 0,1,\ldots N\text{-}1 \tag{11}$$

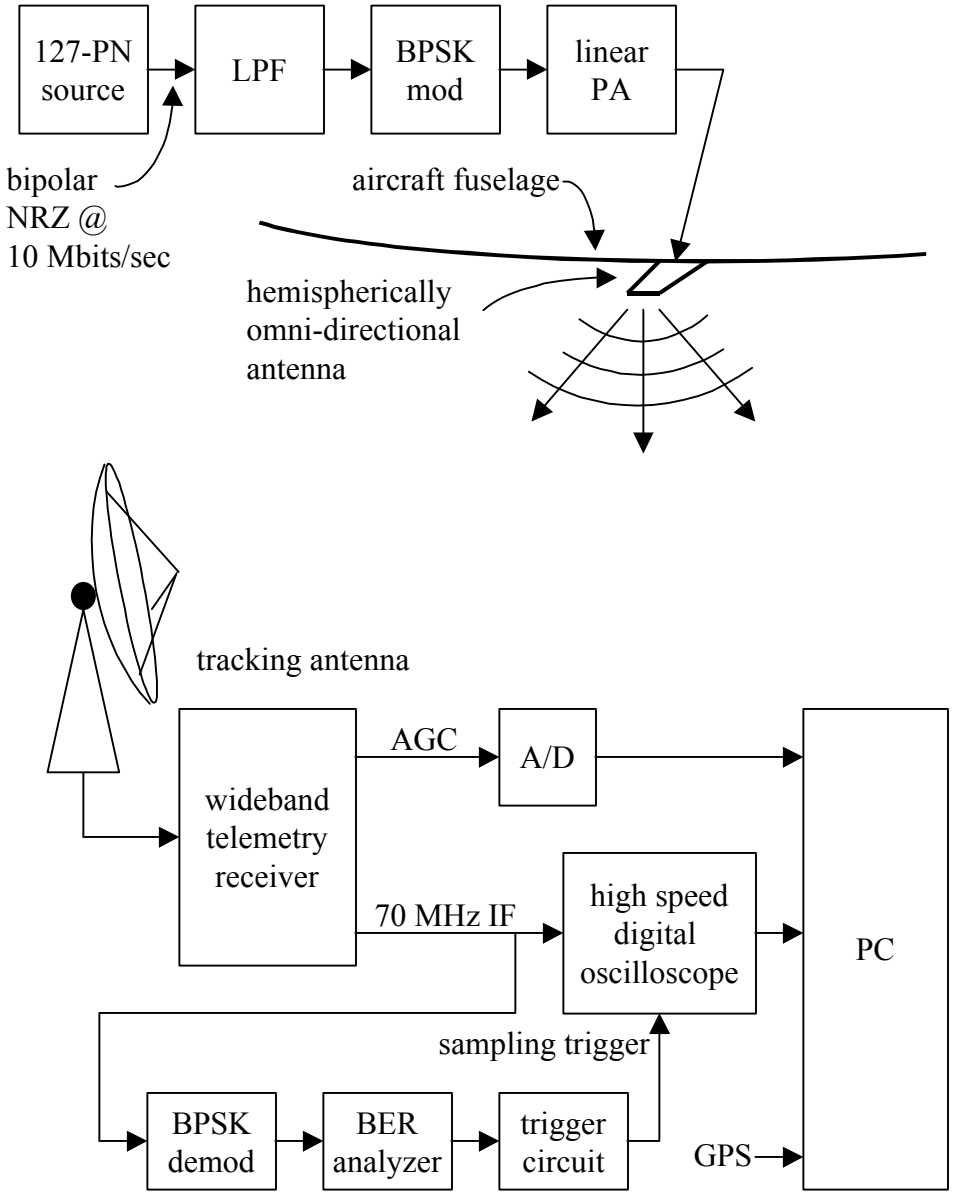

Figure 5: System configuration for the ARTM channel sounding flights.

which are frequency domain samples of $|H(f)|^2$ over those frequencies where $X(f)$ has support [15]. Thus we have

$$\left|H_d\left(e^{j\Omega}\right)\right|^2_{\Omega=\frac{2pk}{N}} = \begin{cases} \left|H\left(\frac{k}{Nt_s}\right)\right|^2 & k = 0,1,...,N/2 \\ \left|H\left(\frac{k-N}{Nt_s}\right)\right|^2 & k = N/2+1,...,N-1 \end{cases} \tag{12}$$

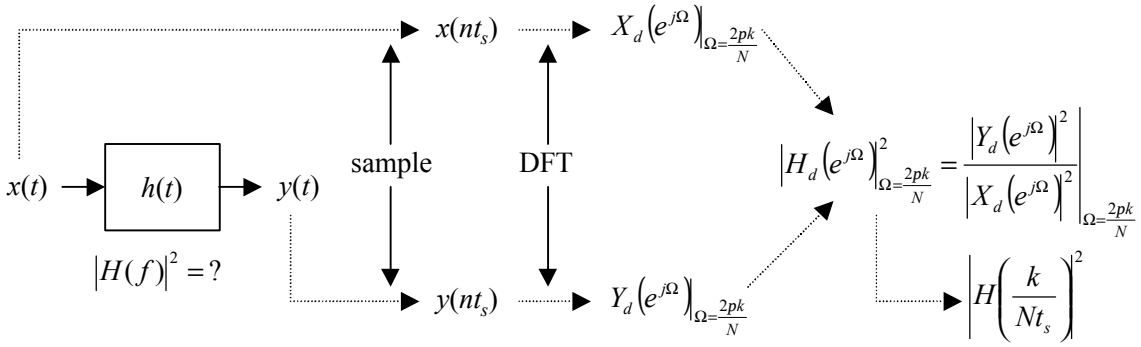

Figure 6: Diagram illustrating the relationship between discrete-time processing and the continuous-time channel impulse response.

Thus while it is impossible to sample $h(t)$ given by (2), (4), or (5) directly (they are not bandlimited signals), it is possible to model samples of $H(f)$ over a limited frequency range [15]. Using the DFT's of the sampled input and output signals and Equation (12) in place of $|H(f)|^2$ in Equation (10), we are able to apply the frequency domain technique to determine the least squares parameters for our channel model using the sampled data.

RESULTS

This paper reports on two of the ARTM channel sounding flights outlined in Table 1. The basic idea of these flights was to gather information from different locations at different frequencies using different receive antennas. This data represents a course sampling of the multipath environments common to land-based aeronautical telemetry and gives us some idea of the number, strength, and delays of the multipath reflections to be expected.

Table 1: Technical specification summaries for ARTM Flights 10 and 11.

ARTM flight identifier	Flight 10	Flight 11
carrier frequency	1510.5 MHz	2344.5 MHz
receive antenna	8-foot parabolic reflector	12-foot parabolic reflector
segment spacing	200 msec	150 msec
flight path	Black Mountain	Cords Road

Some representative curve fits from Flight 10 are illustrated in Figures 7 and 8. These figures also illustrate the data modeling technique using the DFT's of the sampled transmitted and received signals. Figure 7 demonstrates an example where the 2-ray channel model is an excellent match to the data and suggests the existence of a strong specular reflection with a relative amplitude of 0.97 and a differential delay (from the line-of-sight path) of 47 ns. It is clear from the plot in the lower right hand corner that the added complexity of the 3-ray model is unnecessary in modeling this particular data segment. In this case the third ray has a relative amplitude of only 0.04 and could be ignored. Figure 8 is an example where the 3-ray model is required. These results suggest the presence of a strong multipath reflection delayed 74 ns from the line-of-sight signal and a weaker multipath reflection delayed 302 ns from the line-of-sight signal. Both of these examples illustrate an important relationship between the 2- and 3-ray models. The first reflection in the 3-ray model is usually the strong reflection associated with a short delay and is consistent with the reflection modeled by the 2-ray channel model. The second reflection of the 3-ray model is usually a weaker reflection with a long delay. The inclusion of this additional multipath reflection improves the accuracy of the model. Generalizing to L multipaths (see Equation (5)), it is evident that improved modeling accuracy can be realized at the expense of computational complexity. Our experience with these models and the available data suggest that a 3-ray model adequately captures all the essential features of the channel distortions caused by multipath propagation.

The data used in Figure 8 also illustrates an important caveat of channel characterization using the PN cross correlation method. The PN cross correlation for the data of Figure 8 is plotted in Figure 9. The PN cross-correlation data show three peaks at 0 ns (the line-of-sight path), 120 ns, and 370 ns. The 120 ns spacing between the first and second correlation peaks is well below the 200 ns spacing required by the PN correlation method to resolve the individual multipath reflections. The correlation peak at 120 ns is a false correlation peak resulting from the out-of-phase interference between the line-of-sight path and the multipath reflection delayed 74 ns. When the delay between the multipaths is greater than 200 ns, the PN cross correlation method does a nice job of identifying the delay. This is illustrated by the third correlation peak at 370 ns in Figure 9 and is consistent with the frequency domain modeling results in Figure 8.

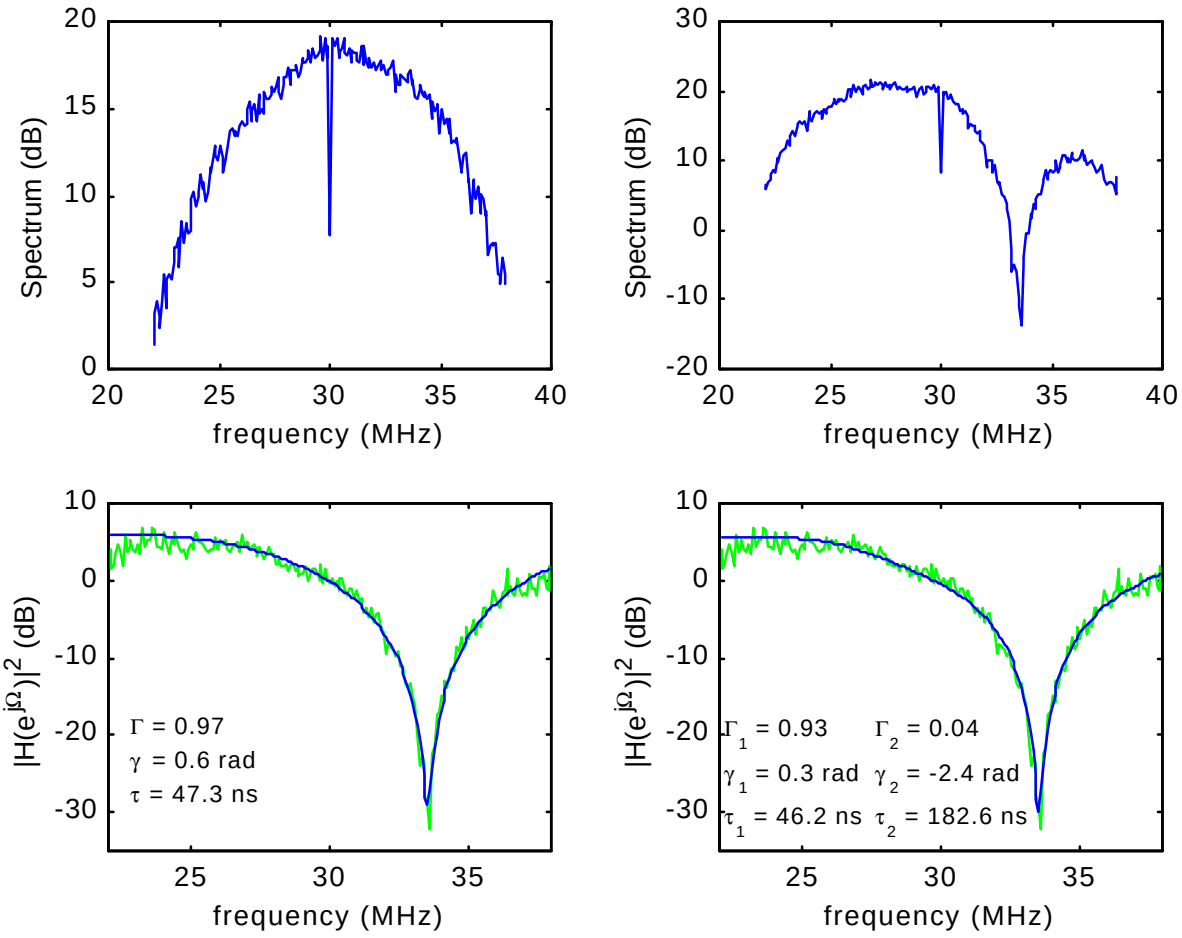

Figure 7: Representative data from Flight 10. This data was recorded during the first segment at time stamp 17:30:11. Starting in the upper left and moving clockwise: (1) the DFT of the transmitted signal; (2) the DFT of the received signal; (3) the resulting sampled channel transfer function together with the least squares curve fit for the 3-ray model; (4) the resulting sampled channel transfer function together with the least squares curve fit for the 2-ray model.

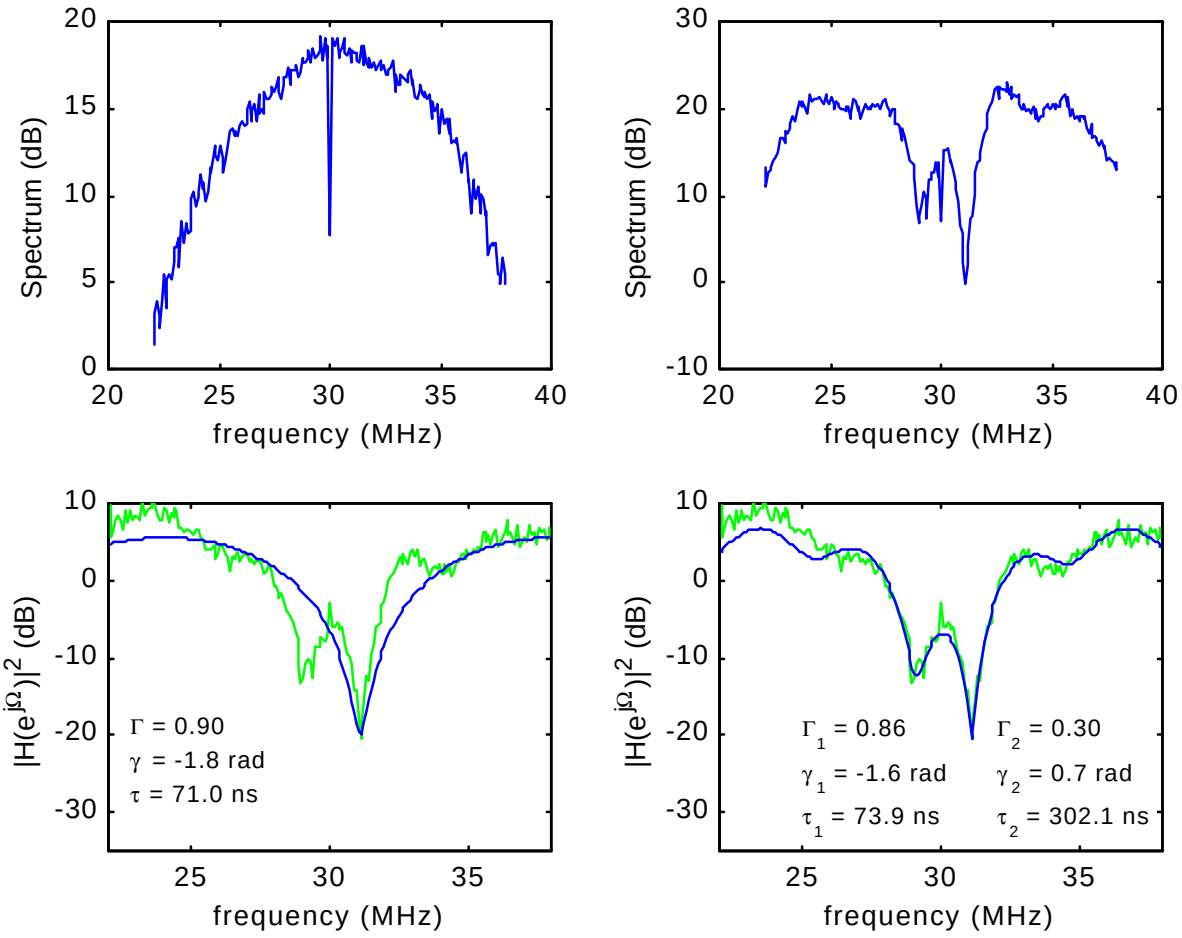

Figure 8: Representative data from Flight 10. This data was recorded during the ninth segment at time stamp 17:30:11. Starting in the upper left and moving clockwise: (1) the DFT of the transmitted signal; (2) the DFT of the received signal; (3) the resulting sampled channel transfer function together with the least squares curve fit for the 3-ray model; (4) the resulting sampled channel transfer function together with the least squares curve fit for the 2-ray model.

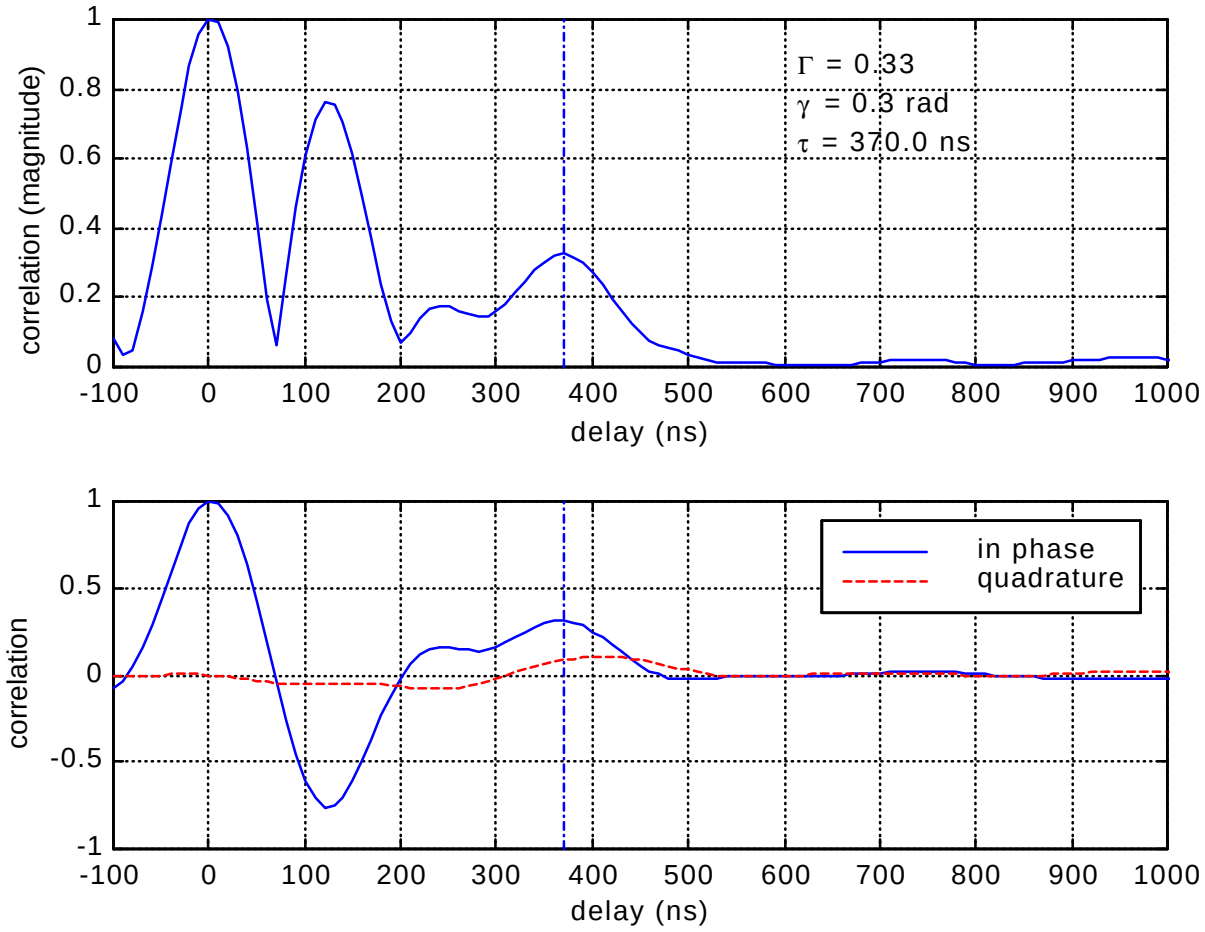

Figure 9: PN cross correlation results for the data presented in Figure 8. These plots are a good example of both the utility and danger of using the PN cross correlation method for the channel parameter estimation. The tallest peak at (normalized) delay 0 ns represents the line-of-sight signal. The frequency domain least-squares curve fits in Figure 8 show that there are two delays accompanying the line-of-sight path. The first delay is a strong delay with relative amplitude 0.86 and relative delay 74 ns. The relative delay is much shorter than the minimum 200 ns spacing required for delay estimation using the PN cross correlation method. In this example, the phase difference between the line-of-sight path and the short-delay path causes a false peak at 120 ns in the correlation. This false peak is obvious in the top plot. The frequency domain least squares curve fit in Figure 8 identifies a second delay with relative amplitude 0.3 and delay 302 ns. This delay is obvious in the correlation curve in the top figure where a peak with relative amplitude 0.33 at 370 ns is observed.

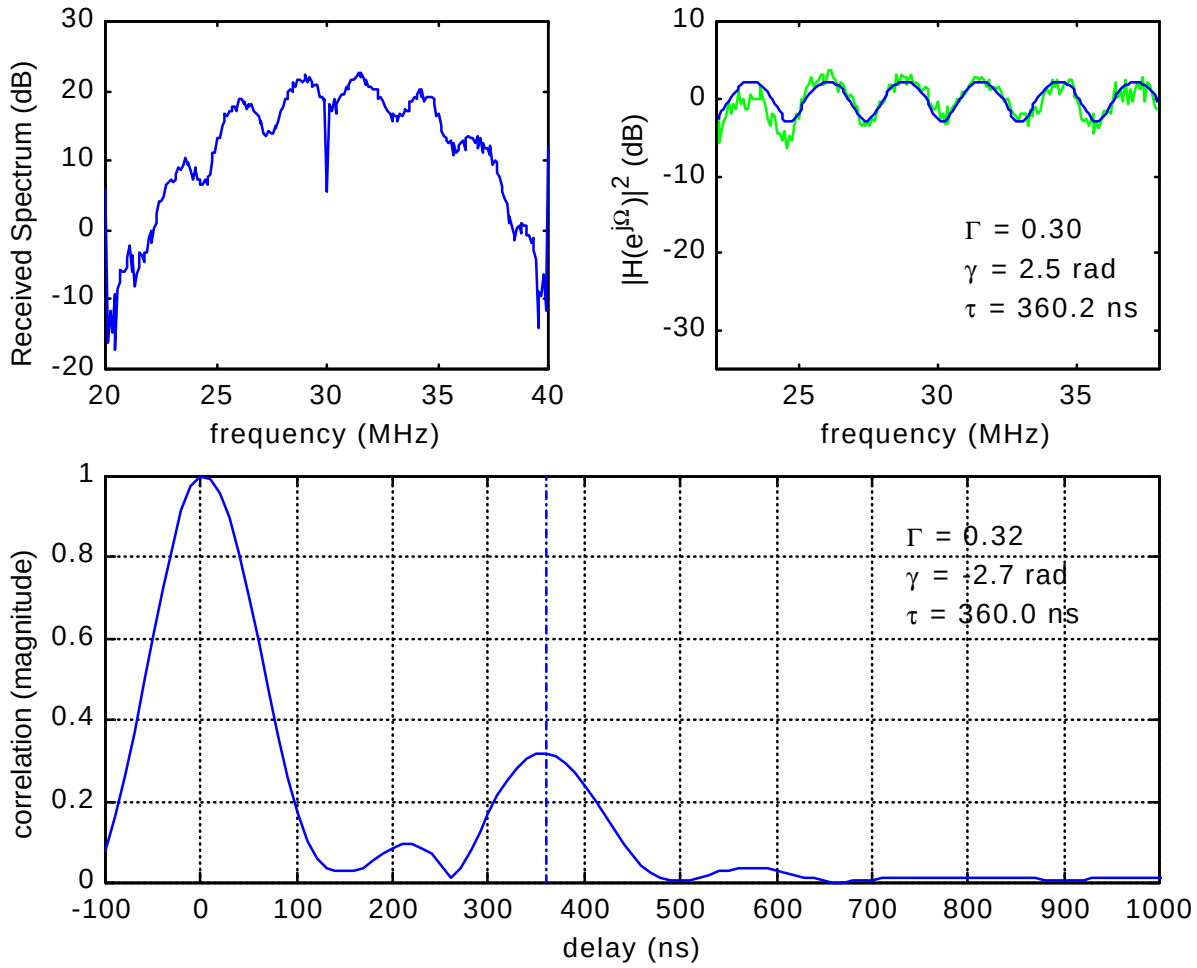

Figure 10: Sample data from Flight 11 showing an example of a long-delay multipath reflection. The upper left plot is the DFT of the received signal (the transmitted signal is identical to the one shown in Figures 7 and 8). The upper right is a plot of the measured transfer function together with a plot of the least squares fit using the 2-ray model. The bottom is a plot of the magnitude of the PN correlation function which shows a correlation peak at 360 ns. Note the close agreement between the frequency domain technique and the PN cross correlation method when the delay is well in excess of 200 ns.

Figure 10 illustrates sample results from Flight 11. This plot is an example of a long multipath delay of 360 ns. As expected, a multipath characterized by a delay this long has a relative amplitude which is smaller than the relative amplitudes associated with short-delay multipath reflections. The frequency domain and PN cross-correlation methods produce very similar results. This reinforces our confidence in the modeling results obtained using the frequency domain technique.

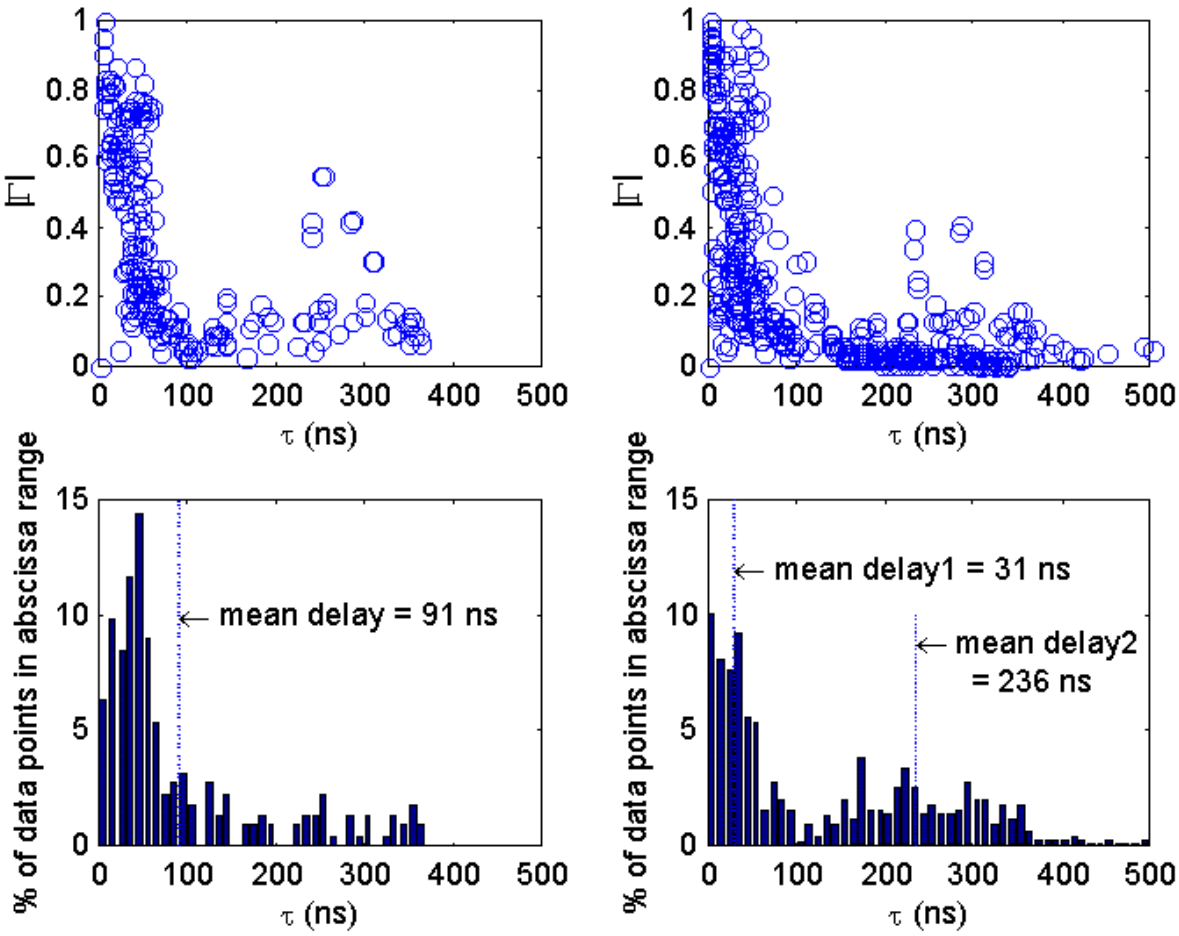

Figure 11: Parameter summaries of the 2-ray model (left column) and 3-ray model (right column) for the Black Mountain Run (ARTM Flight 10) at Edwards AFB with an aircraft at an altitude of 5,000 feet.

Figures 11 through 14 summarize the 2- and 3-ray modeling results using the frequency-domain technique. Figures 11 and 12 summarize the results from Flight 10 at L-band while Figures 13 and 14 summarize the results from Flight 11 at S-band. We make the following observations:

General Form for the Channel Model: In general, we observe two multipath reflections together with the line-of-sight signal. The first multipath is a strong specular reflection with relative amplitude greater than 0.5 and relative delay in the 30 to 70 ns range. The second multipath is a much weaker reflection with relative amplitude less than 0.5 and relative delay in the 175 to 325 ns range. To demonstrate that these numbers are reasonable, we consider the cross sectional slice of terrain for Flight 10 at time 17:30:11 (the high-altitude Black Mountain run) shown in Figure 15. The differential path delays for a single multipath reflection with reflection points A, B, and C as shown were computed. The differential delay assuming a reflection from point A (the edge of the 3-dB antenna beamwidth) is 28 ns. The differential delay assuming a reflection from point

B is 231 ns while the differential delay assuming a reflection from point C is 5855 ns. These values bound the possible delays of multipath reflections from

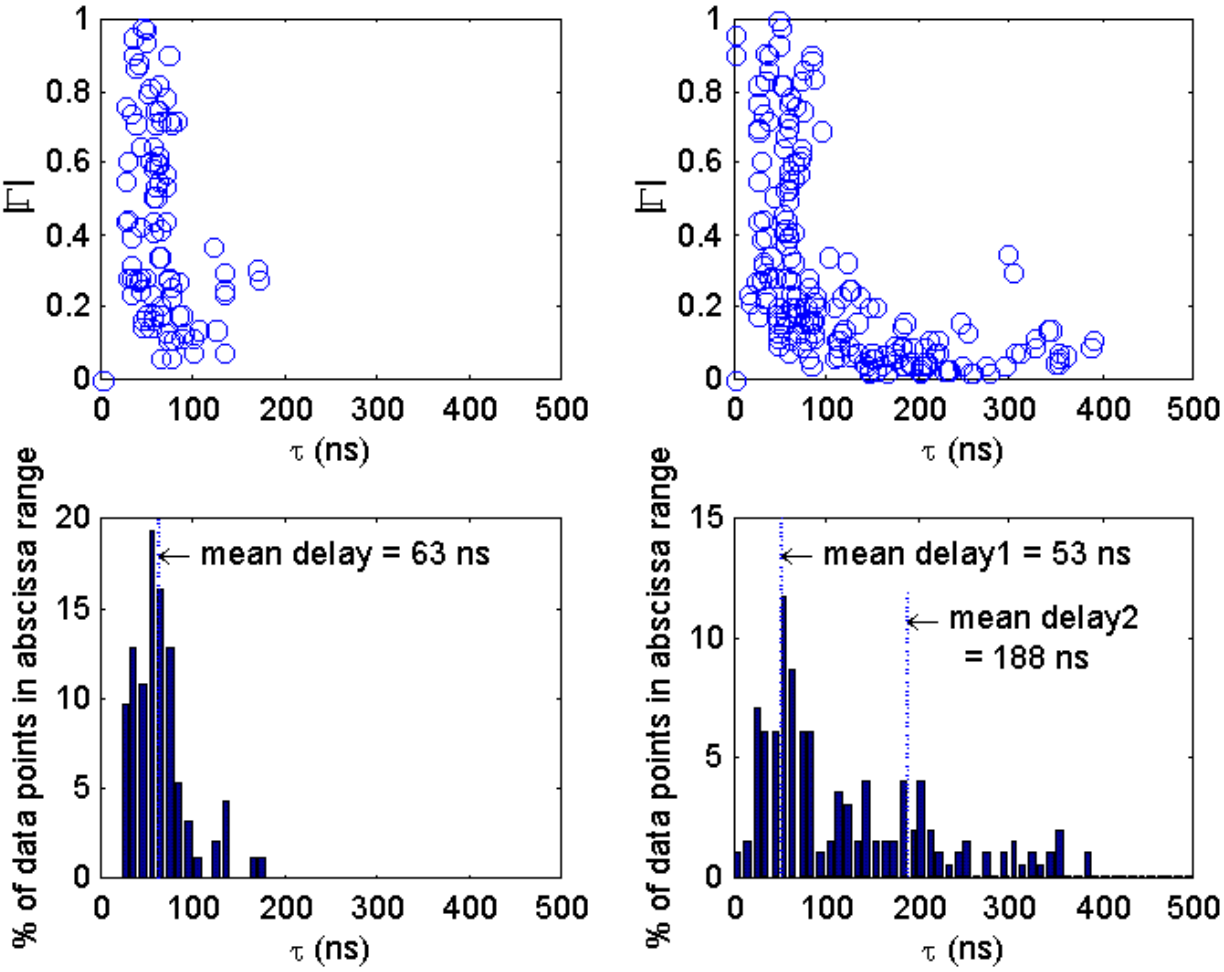

Figure 12: Parameter summaries for the 2-ray model (left column) and 3-ray model (right column) for the Black Mountain Run (ARTM Flight 10) at Edwards AFB with an aircraft at an altitude of 10,000 feet.

the ground at this point in the test flight. The modeling results summarized in Figure 8 are within this range . Note that for the data modeled in Figure 8, we see that the strong, short-delay reflection occurs off the dry lake bed approximately half way between the aircraft and the receiver while the weak, long-delay reflection occurs in the foothills of the Black Mountains.

Amplitude-Delay Relationship: In general, strong multipaths are characterized by short delays on the order of 50 ns. Multipath reflections with longer relative delays on the order of 200 to 300 ns are much weaker. This is to be expected since the longer paths that lead to longer delays usually impose greater attenuation.

Frequency Dependency: Given the limited data available at this time, it is difficult to determine which differences in Figures 11 through 14 are frequency dependent and which are geometry dependent. Figures 13 and 14 demonstrate that there is tremendous

variation over a single flight path. Even though the frequencies and flight paths were different, the results from the curve fitting at the two frequencies are quite similar. It is clear that there is significant multipath interference at both the L- and S-bands.

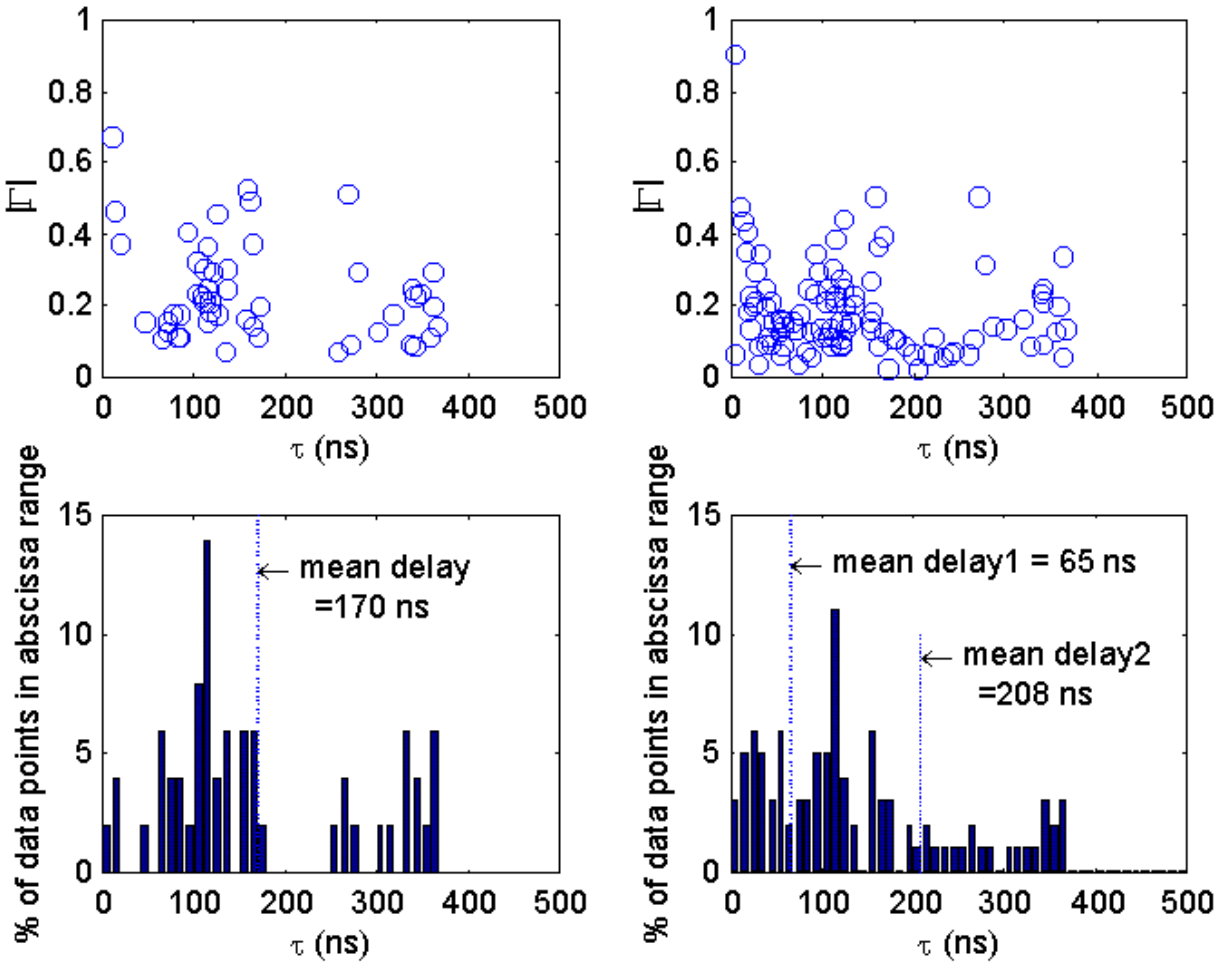

Figure 13: Parameter summaries for the 2-ray model (left column) and 3-ray model (right column) for the middle portion of the Cords Road Run (ARTM Flight 11) at Edwards AFB with an aircraft at an altitude of 4,200 feet.

Altitude Dependency: An interesting relationship exists between transmitter altitude and channel characteristics. Figure 11 summarizes the results for the Black Mountain run for an aircraft at an altitude of 5,000 ft while Figure 12 summarizes the results for the same flight path for an aircraft at an altitude of 10,000 ft. The low altitude run exhibited long delays on the order of 200 to 300 ns which are completely absent in the high altitude run. With a few exceptions, we see that the long-delay multipaths are weak reflections with a relative amplitude of 0.2 or less. During the high altitude runs, the increased attenuation due to the higher altitude and different incidence angles resulted in multipaths too weak to trigger a data acquisition event.

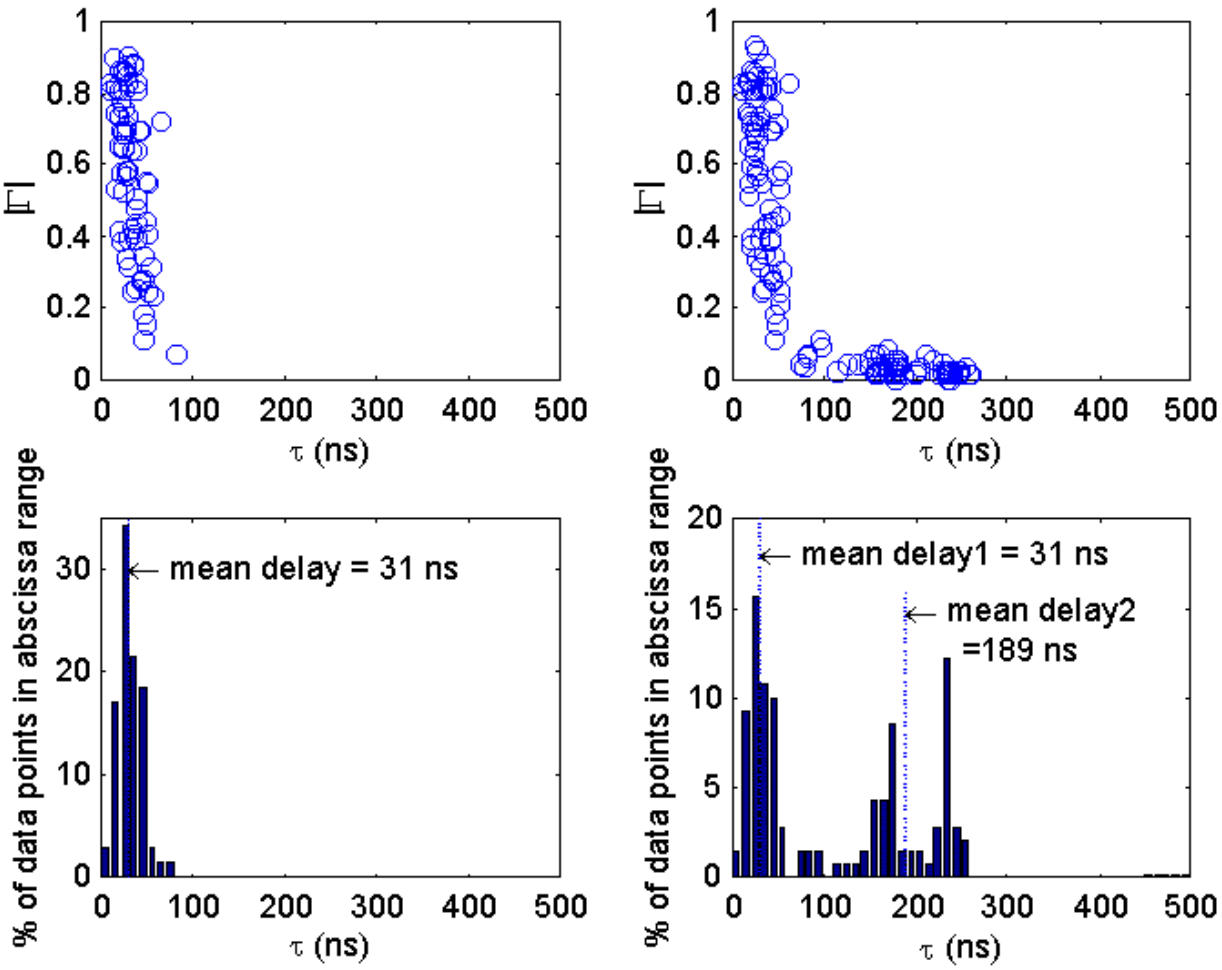

Figure 14: Parameter summaries for the 2-ray model (left column) and 3-ray model (right column) for the east-most portion of the Cords Road Run (ARTM Flight 11) at Edwards AFB with an aircraft at an altitude of 4,500 feet.

Relationship to Bit Error Rate: Figures 16 and 17 present the bit error count together with the channel sounding trigger events on the same time axis. The plot facilitates a correlation between channel conditions and the recorded bit errors. The event numbers below the trigger events are a key in cross-referencing the channel conditions summarized in Tables 2 and 3. For the sake of brevity, the tables list average values for the 2-ray model least-squares fit parameters. In general, the large amplitude reflections cause the largest increases in bit error rates. This is to be expected. What these figures suggest is that even relatively small multipath reflections with amplitudes 0.3 or less can cause significant increases in the bit error rate.

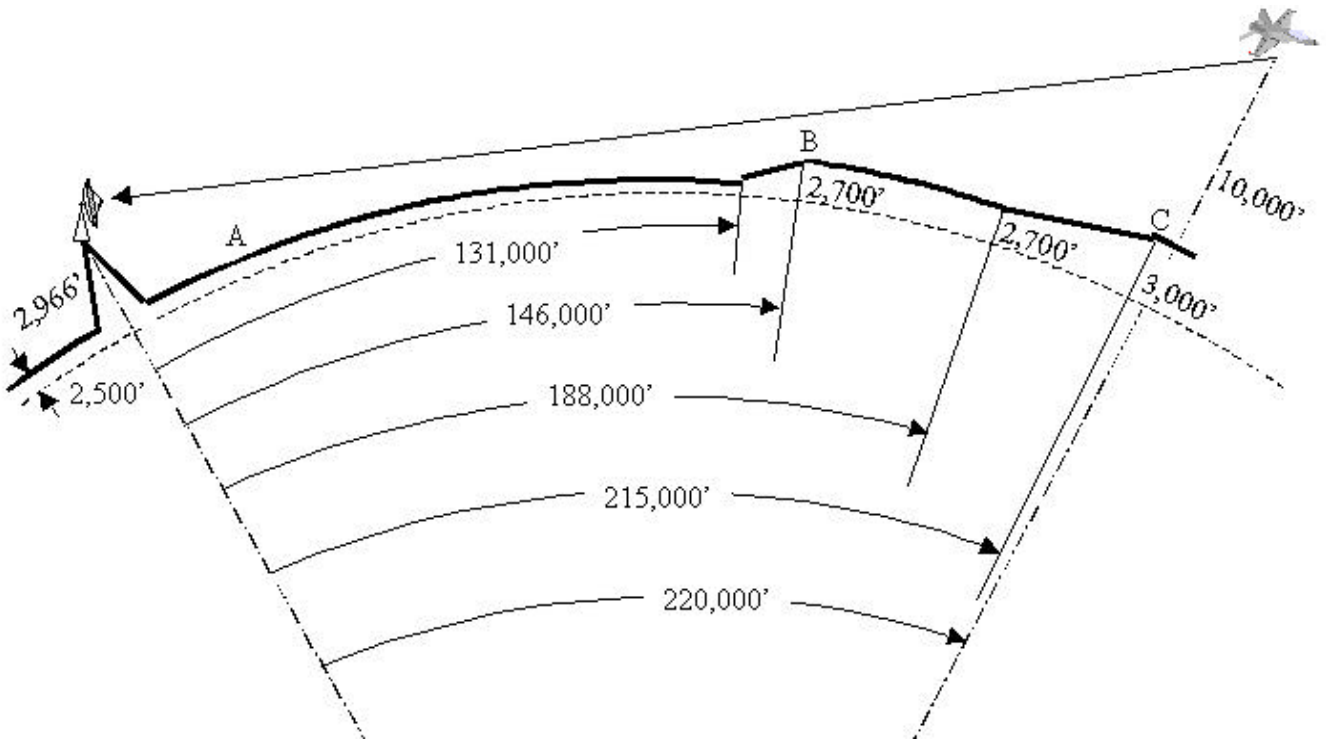

Figure 15: Cross-section of the aircraft-to-ground station terrain for Flight 10, time 17:30:11. The vertical scale is exaggerated to show the terrain features where the elevations are indicated. The line-of-sight path is shown as the solid line from the aircraft to the ground station. The differential delay for a single multipath reflection for 3 different reflection points is computed: point A, the edge of the 3-dB beam width; point B, the edge of the low hill overlooking the dry lake bed; point C, near the top of the Black Mountains directly under the aircraft. The differential delays are 28 ns for point A, 231 ns for point B, and 5855 ns for point C.

CONCLUSIONS

We have summarized results from two ARTM channel sounding experiments designed to provide a course sampling of the terrain and frequencies typical of land-based aeronautical telemetry. Channel modeling was performed in both the time-domain (PN cross correlation) and frequency domain (least squares curve fit to an assumed model). The two methods provided consistent results when the differential path delays exceeded 200 ns. We demonstrated that the channel parameters derived from this analysis were within the bounds imposed by the transmitter-to-receiver geometry. It is shown that 2-ray and 3-ray multipath models provide an excellent match to the data obtained thus far. The 3-ray model is characterized by a strong line-of-sight propagation path; a strong short-delay specular reflection with relative amplitude greater than 0.5 and delay in the 30 to 70 ns range; and a weaker, long delay specular reflection with relative amplitude less than 0.5 and delay in the 175 to 325 ns range. Finally, we demonstrated the correlation

between channel parameters and bit error rates. This analysis showed that that the magnitude of the reflection is the dominant factor in determining bit error rate.

Table 2: Summary of average best-fit parameters for the 2-ray model using data from Flight 10. The event numbers correspond to the numbers marked in Figure 16. The measured BER is the average BER over the interval during which the 10 data segments were recorded.

Event number	average Γ	average τ (ns)	measured BER
1	0.32	297	4.0×10^{-3}
2	0.28	46	9.0×10^{-7}
3	0.29	61	3.8×10^{-6}
4	0.10	349	7.0×10^{-7}
5	0.46	26	1.2×10^{-3}
6	0.76	45	2.3×10^{-6}
7	0.27	24	1.9×10^{-6}
8	0.35	50	1.5×10^{-6}
9	0.75	50	8.2×10^{-3}
10	0.51	22	1.0×10^{-5}

Table 3: Summary of average best-fit parameters for the 2-ray model using data from Flight 11. The event numbers correspond to the numbers marked in Figure 17. The measured BER is the average BER over the interval during which the 10 data segments were recorded.

Event number	average Γ	average τ (ns)	measured BER
1	0.29	156	9.1×10^{-2}
2	0.46	124	2.0×10^{-4}
3	0.25	360	6.0×10^{-4}
4	0.16	308	4.0×10^{-4}
5	0.85	26	6.9×10^{-1}
6	0.76	17	3.3×10^{-1}
7	0.79	15	8.6×10^{-1}
8	0.70	38	6.6×10^{-1}
9	0.65	41	5.0×10^{-1}
10	0.70	26	5.5×10^{-1}
11	0.53	42	8.7×10^{-1}

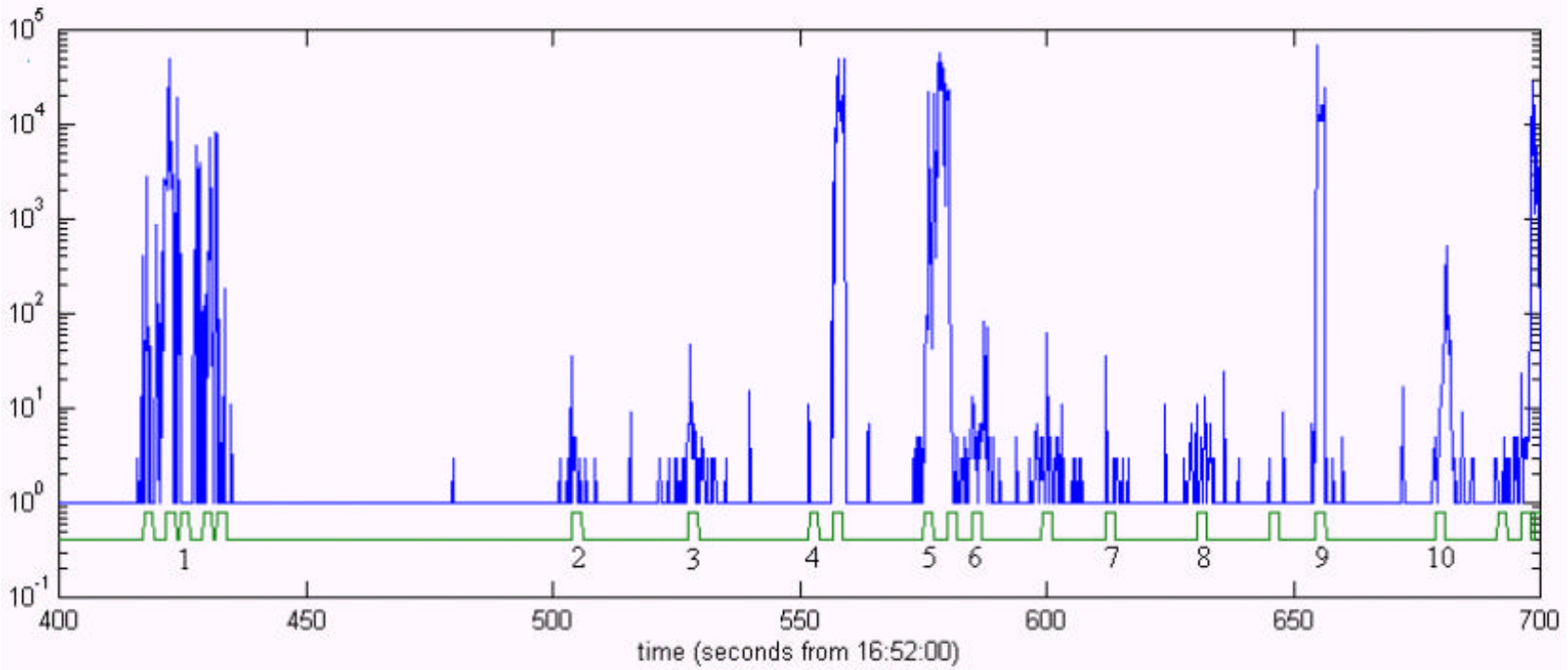

Figure 16: Correlation between recorded bit error counts and channel conditions for the first part of the low-altitude Black Mountain Run from Flight 10. Each point on the top line is a one plus the number of bit errors recorded by the bit error rate analyzer during a 200 ms interval. The lower line plots the trigger events for the digital oscilloscope. The trigger events allow us to perform a time correlation between bit error rate and recorded channel outputs. The event numbers below the trigger events are a key in cross-referencing the channel conditions summarized in Table 2. Note that event numbers 2, 3, 4, 7, and 8 correspond to channel conditions characterized by multipath reflections with relative amplitudes less than 0.3 and include both long (greater than 100 ns) and short (less than 100 ns) delays. Thus we see that even weak multipath can cause significant BER performance degradation.

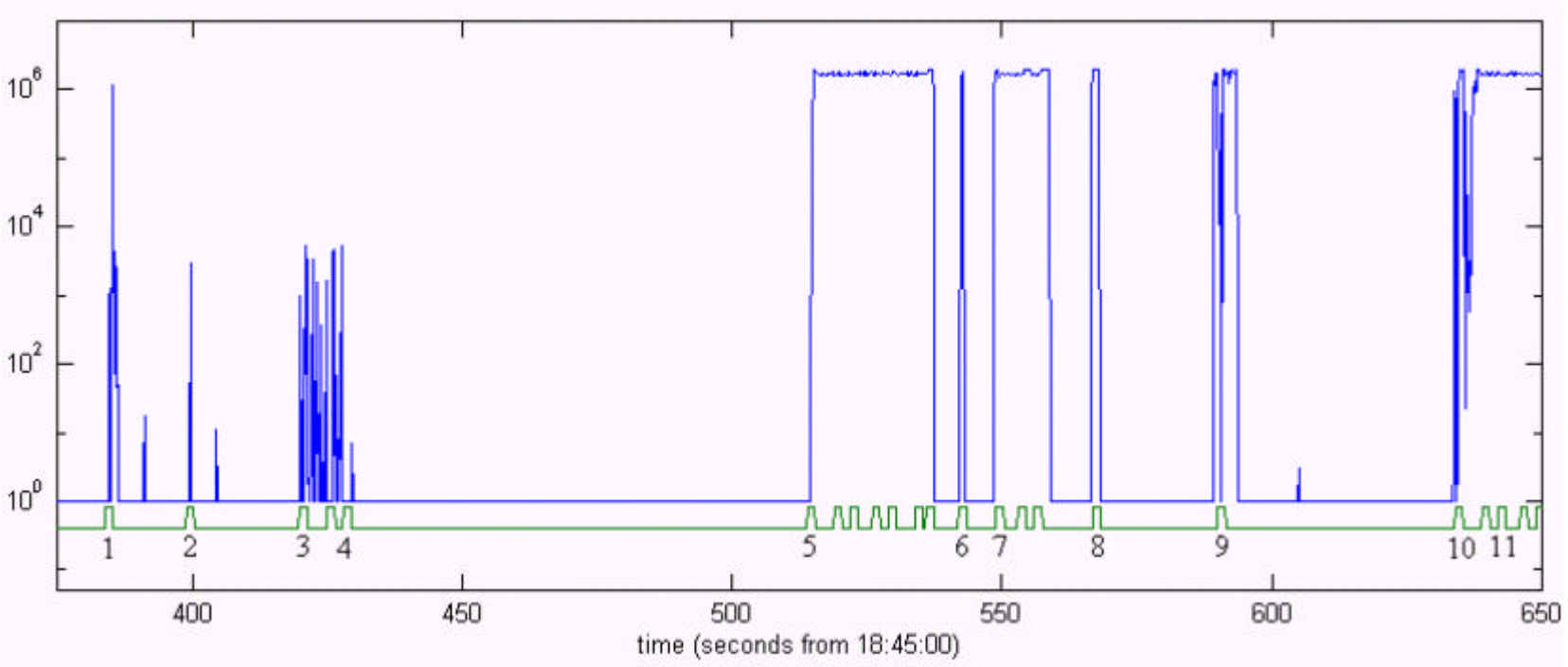

Figure 17: Correlation between recorded bit error counts and the channel conditions for the Cords Road Run from Flight 11. Each point in the top line is the number of bit errors recorded by the bit error rate analyzer during a 150 ms interval. The lower line plots the trigger events for the digital oscilloscope. The trigger events allow us to perform a time correlation between bit error rate and recorded channel outputs. The event numbers below the trigger events are a key in cross-referencing the channel conditions summarized in Table 3. Event numbers 1-4 occurred when the aircraft was at the mid-point of the Cords Road run. At this point, the channel is characterized by long delays (longer than the 100 ns bit time) and amplitudes less than 0.5. Event numbers 5 –11 occurred when the aircraft was at the eastern end of the Cords Road run where the channel is characterized by short delays (less than half the 100 ns bit time) and amplitudes greater than 0.5. This plot illustrates clearly that the shorter, stronger delays degrade BER performance much more than the weaker, longer delays.

REFERENCES

1. Rice, M. and E. Law, "Aeronautical Telemetry Fading Sources as Test Ranges," in Proceedings of the International Telemetering Conference, volume 33, Las Vegas, Nevada, October 1997, pages 287—293.
2. Jakes, W., Microwave Mobile Communications, IEEE Press, Piscataway, New Jersey, 1974.
3. Proakis, J., Digital Communications, Third Edition, McGraw-Hill, New York, 1995.
4. Landon, D. "Doppler Bandwidth Characterization of ARTM Channel Sounding Data," in Proceedings of the International Telemetering Conference, volume 35, Las Vegas, Nevada, October 1999.
5. Bishop B. and E. Law, "S and L Telemetry Bands: Signal Level Comparison," Technical Report, Point Mugu, California, October 11, 1973.
6. Law, E., private communication, Naval Air Weapons Center WPNS, Point Mugu, California.
7. Law, E., "Performance of PCM/FM During Frequency Selective Fading," in Proceedings of the International Telemetering Conference, volume 31, Las Vegas, Nevada, October 1995, pages 224—231.
8. Reddemann, J., "Edwards Range Telemetry Evaluation," in Proceedings of the International Test and Evaluation Conference, Lancaster, California, April 1997.
9. Friend, D., "BER Analysis of an F-16 Test Run at Edwards AFB," in Proceedings of the International Telemetering Conference, volume 33, Las Vegas, Nevada, October 1997, pages 619—624.
10. Welling, K., "Analysis of JDAM Tests at China Lake," in Proceedings of the International Telemetering Conference, volume 33, Las Vegas, Nevada, October 1997, pages 521—528.
11. Balanis, C., Advanced Engineering Electromagnetics, John Wiley and Sons, New York, 1989.
12. Rice, M. and D. Friend, "Antenna Gain Pattern Effects on Multipath Interference in Aeronautical Telemetering," in Proceedings of the International Telemetering Conference, volume 33, Las Vegas, Nevada, October 1997, pages 113—120.
13. Peterson, R. and R. Ziemer and D. Borth, Introduction to Spread Spectrum Communications, Prentice-Hall, Englewood Cliffs, New Jersey, 1995.
14. Rummler, W., "A New Selective Fading Model: Application to Propagation Data," Bell System Technical Journal, volumn 58, July-August, 1979, pages 1037—1071.
15. Oppenheim, A. and A. Willsky, Signals and Systems, Second Edition, Prentice-Hall, Upper Saddle River, New Jersey, 1997.